PNAS RESEARCH ARTICLE | BIOPHYSICS AND COMPUTATIONAL BIOLOGY

Stochastic motility energetics reveals cooperative bacterial swarming in optical tweezers

Clara Luque-Rioja[a,b], Horacio López-Menéndez[a,c], Macarena Calero[a,b,d,e], Niccolò Caselli[a,b], Diego Herráez-Aguilar[b,f], Juan Pedro G. Villaluenga[g,1], and Francisco Monroy[a,b,1]

Affiliations are included on p. 10.

Edited by Simone Pigolotti, Okinawa Kagaku Gijustu Daigakuin Daigaku, Onna, Japan; received June 11, 2025; accepted December 8, 2025 by Editorial Board Member Christopher Jarzynski

Bacterial flagellar swarming enables dense microbial populations to migrate collectively across surfaces, often resulting in emergent, coordinated behaviors. However, probing the underlying energetics of swarming at the single-cluster level remains a challenge. Here, we combine optical tweezers and multiparticle tracking within a stochastic thermodynamic framework to characterize the active motility of confined *Proteus mirabilis* clusters. Using the photon momentum method to directly measure trapping forces, we show that swarming clusters generate persistent, dissipative flows indicative of nonequilibrium stationary motility within confined solenoidal mesostructures. These flagellar rotational dynamics break detailed balance in mesoscopic force space and exceed the limits of passive friction, as evidenced by force-velocity correlations and vortex-like circulations. By coarse-graining cluster trajectories into an active Brownian phase space, we quantify the work performed by bacterial swarms at cooperative coupling to thermal fluctuations, resulting in dissipative Ohmic-like currents overcoming conservative trapping. Our findings establish a generalizable approach to quantify collective motility and energetic dissipation in active bacterial clusters under confinement, offering insights into the physical principles governing microbial cooperativity.

stochastic energetics | Brownian stochasticity | microbial swarming | entropy production

Significance

Microscopic randomness, consistency, and adaptability are core features of living systems, yet difficult to quantify in biological collectives. *Proteus mirabilis*-among the fastest known swarming bacteria, provides a unique opportunity to investigate these principles under microphysical constraints. Using stochastic thermodynamics in an optical tweezer setting, we show that confined bacterial clusters undergo cooperative Brownian motion driven by flagellar activity: Motile bacteria adaptively synchronize into mesoscopically persistent force currents, reducing dissipation while preserving thermodynamic consistency. This cooperation reveals how bacterial swarms optimize microscopic energy use when confronted with environmental noise under tight confinement.

In nature, nonequilibrium arises from persistent energy imbalances between systems and their surroundings (1, 2). Power-consuming systems operating in fluctuating environments, such as living organisms, are thus constrained by fundamental limits on thermodynamic efficiency (3). Within the framework of stochastic energetics (4), these bounds remain valid even when systems exhibit Brownian-like diffusivity while maintaining nonequilibrium steady states (NESS) (5–10). In NESS, thermal and active fluctuations coexist, persistently breaking detailed balance through correlated forcing that overcomes friction (7, 11). Despite their irreversibility, these mechanical transitions remain thermodynamically consistent at mesoscopic scales, in accordance with stochastic energetics (4, 12). NESS are characterized by continuous energy fluxes -as entropy production (13), which quantifies the degree of irreversibility and governs power dissipation through stochastic fluctuations (10, 14, 15). Thermodynamic performance in such systems involves minimizing frictional dissipation (5), while sustaining a positive entropy production (6, 13, 15, 16), consistent with adaptive multiscale responses observed in biological systems (17–22). Indeed, physiological energy use is multiscalar, with only a tiny fraction of metabolic input appearing as emergent flows (23), a distinction clarified by the stochastic thermodynamics of small systems (5–7).

Microbial motility—including flagellar cell swimming, collective swarming, and chemotactic migration, illustrates these principles emerging as a canonical example of mesoscopic NESS constrained by fluctuating energetic landscapes (24). The nonreciprocal in-milieu propulsion enables robust microbial adaptation to variable environments under thermal noise (24–26). Hence, motion efficiency in microbial collectives depends on their thermodynamic consistency (24), mediated by the coupling of metabolic power input, frictional resistance, and resulting entropy production (27, 28). Bacterial cooperativity may thus be arise as an optimized NESS, balancing dissipation with adaptivity under environmental randomness (29, 30). Flagellated microbes are highly efficient at converting metabolic energy into swimming motion (31). Their rotary motors -powered by chemical gradients under ATP consumption, are among the most complex molecular machines in biology (32, 33), with evolved function

Author contributions: F.M. designed research; C.L.-R., H.L.-M., M.C., N.C., D.H.-A., and F.M. performed research; M.C., N.C., D.H.-A., J.P.G.V., and F.M. contributed new reagents/analytic tools; C.L.-R., H.L.-M., D.H.-A., J.P.G.V., and F.M. analyzed data; and J.P.G.V. and F.M. wrote the paper.

The authors declare no competing interest.

This article is a PNAS Direct Submission. S.P. is a guest editor invited by the Editorial Board.

[1]To whom correspondence may be addressed. Email: jpgarcia@ucm.es or monroy@ucm.es.

This article contains supporting information online at https://www.pnas.org/lookup/suppl/doi:10.1073/pnas.2515129123/-/DCSupplemental.

Published January 16, 2026.

adaptive to environmental responsiveness (34). While the biochemical basis of flagellar motility is well established (35), its energetic cost has mainly been inferred from indirect methods, including microcalorimetry, hydrodynamic analyses, and computational modeling (27, 36–40). Jones et al. (41) used optical tweezers (OT) with the photon momentum method (PMM) (42–44) to measure mesoscopic forces in biflagellated algae *Chlamydomonas reinhardtii*, revealing confined oscillations associated with its *run-and-tumble* motility (45, 46). They quantified power dissipation up to $10^6 k_B T/\mathrm{s}$ ($\approx fW$), highlighting the energetic cost of breaststroke-driven propulsion. Later, Battle et al. (11) showed that *Chlamydomonas* flagellar beating breaks detailed balance, with coarse-grained phase-space (CGPS) fluxes revealing mesoscopic NESS arising from fluctuation–dissipation violations (5–7). Despite this existing knowledge, direct measurements of collective motility during bacterial swarming remain largely unexplored, particularly when multiple motors operate within clustered cells. Although individual bacteria can be visually tracked (47), the limited number of trajectory samples constrains thermodynamic analysis (48), rendering microscopic investigations inaccessible (20, 22). Averaging over multiple single-cell trajectories is yet required for thermodynamic consistency (4), but this can obscure details of mesoscopic motion (7, 49), a gap critical for understanding flagellar efficiency in bacterial clusters (27).

The photon momentum method (PMM) enables direct measurement of ensemble-averaged forces without assuming a specific mesoscopic displacement model (e.g., a linear spring) (43). By combining PMM-based optical tweezers (PMM-OT) (42–44, 50) with multiple-particle tracking (MPT) (51–53), we achieve precise quantification of motility-induced work in trap-confined environments (26, 54, 55). PMM-OT/MPT allows evaluation of absolute work along center-of-mass trajectories (41), supported by displacement acquisition through imaging (47, 48). With subpiconewton sensitivity and kilohertz sampling, this approach resolves mechanical forces and dissipation during bacterial motility, providing insights into the thermodynamics of active systems. When integrated with a stochastic CGPS framework, this method quantifies flagellum-driven swarming under thermal noise without relying on linear force–displacement assumptions. Unlike traditional calibration-based approaches, PMM-OT/MPT captures real-time stochastic work fluctuations in nonequilibrium steady states (NESS), enabling direct assessment of active mechanical dissipation in bacterial clusters. At its core, our study asks: *How much energy do bacteria expend to move collectively?* Similar to bird flocks or bee swarms, bacterial collectives should achieve NESS efficiency through cooperation. Using optical tweezers and stochastic thermodynamics, we probe this trade-off, linking flagellar activity to emergent flows under confinement.

Motility Setup: Bacterial Swarms. In this work, we focus on *Proteus mirabilis*, a facultatively anaerobic, Gram-negative bacterium common in soil and water (56), selected for its exceptional motility (57, 58). An opportunistic pathogen causing wound, urinary, and septic infections (56), it is often antibiotic-resistant (59). Its genus name, derived from the shape-shifting Greek god *Proteus*, reflects its adaptive ability to alter morphology and motility in response to environmental conditions (60). *P. mirabilis* swims efficiently in liquid media as a short rod-shaped *bacillus* (1 μm long, 0.5 μm wide) equipped with 4-10 flagella, reaching peak speeds of $c_S \approx 20\,\mu\mathrm{m/s}$ (56). In viscous gels, free swimming is suppressed (61), promoting confined swarming, while on solid surfaces, cells elongate, hyperflagellate, and migrate collectively (58, 60). Flagellar mechanics constrains single-cell energetics (24, 37), but collective motion involves hidden internal degrees of freedom and metabolic consistency as regulatory adaptations to mechanical cues (31, 32).

As a proof of concept, we confined live *P. mirabilis* clusters in optical tweezers and quantified motility with photon momentum force detection (PMM-OT) (44) and high-resolution MPT (52, 53). Trapped clusters exhibited coordinated vortex-like motion-*like a swarm within a hive* (Fig. 1 and Movie S1), consistent with active Brownian dynamics (28). From stationary NESS trajectories (62), we computed motility work from center-of-mass displacements and optical forces (41). This stochastic energetics framework shows how internal dissipation sustains collective propulsion against trapping, revealing power-friction imbalances that constrain the thermodynamic efficiency of flagellar cooperativity in fluctuating microenvironments. Here, swarming refers not to colony-scale spreading but to minimal cooperative clusters isolated under optical confinement in the mesoscale. This reductionism provides a microphysical laboratory that complements ecological assays, enabling bona fide force and dissipation measurements that link microscopic cooperativity to macroscopic swarm behavior.

Results

As shown in Fig. 1, we studied the confined motion of *P. mirabilis* by trapping single cells and assembling them into

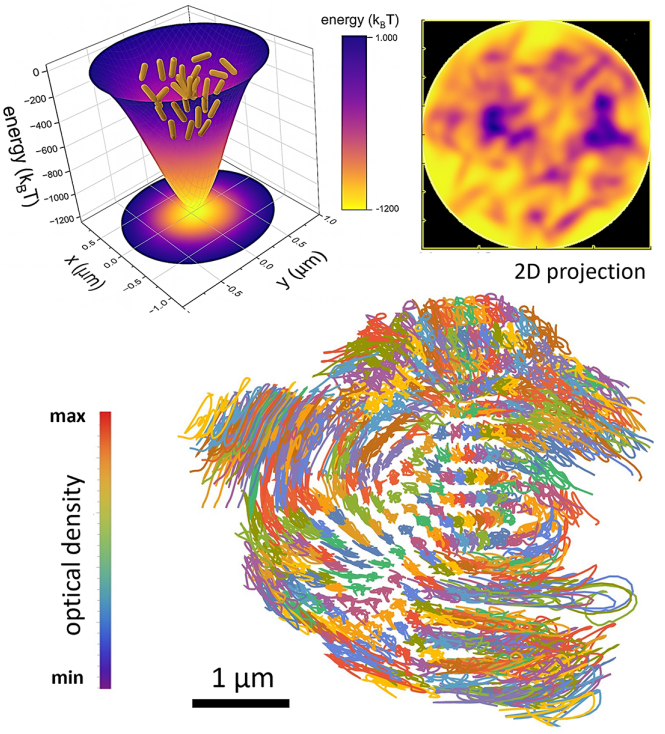

Fig. 1. Bacterial swarming motion detected via Multiple Particle Tracking (MPT) in a single optical tweezer. *Upper* panels: 3D energy cup of the optical trap obtained from experimental calibration force profiles (*SI Appendix*, Fig. S2) with confined bacteria (*Left*) and schematic 2D x-y density projection used for tracking (*Right*, see Movie S1). MPT trajectories of the confined bacterial cluster (main panel). Each detectable "particle" is tracked to infer global center-of-mass motion (*Materials and Methods*). Core-confined particles show Brownian motion with collective rotation, while peripheral particles travel longer distances driven by flagellar strokes. The color map indicates particle masses inferred from optical densities.

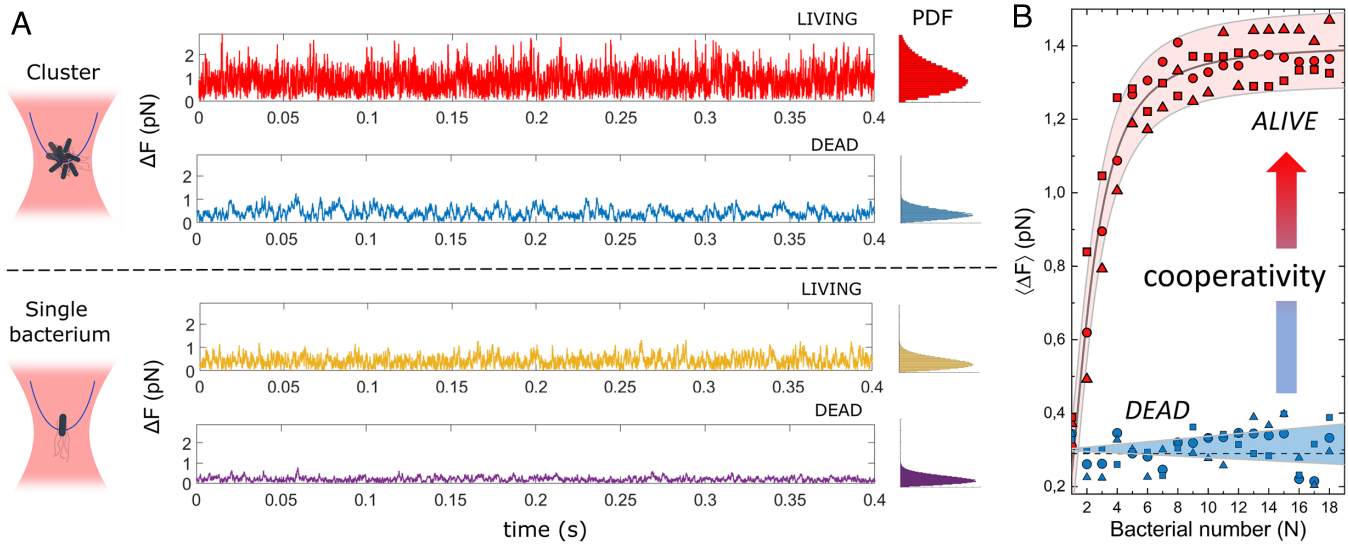

Fig. 2. Optical tweezers with the photon momentum method (OT-PMM) for trapping *P. mirabilis* bacteria. Experimental conditions: laser power, 23*mW* in sample; trapping stiffness, $k = 16$ to 20 pN/μm; solvent viscosity, $\eta = 10^{-3}$ kg/(m·s); at room temperature, $T = 22$ °C: (*A*) Fluctuating force realizations for living and dead systems over time, $\delta F(t)$ (*Central* panels): clusters (*Top*); single bacteria (*Bottom*). Force probability distributions follow Maxwellian modulus statistics, $P(F) \propto (F^2/\Delta F^2) exp(-F^2/2\Delta F^2)$, with an effective force variance $\Delta F^2 \propto k_B T_{eff}$ (PDFs; *Right* panels). (*B*) Realization-averaged fluctuating force $\langle \Delta F(N) \rangle \equiv (\delta F^2)^{1/2}$ as a function of the number of bacteria aggregated into trapped clusters (N). Motile bacteria trapped alive (red); dead bacteria under fixation (blue). Symbols represent different aggregation sequences. Swarming cooperativity is observed as a logistic increase in motility forces, indicating functional binding among clustered living bacteria. The solid line represents the best fit to a Hill function (Eq. **1**) with a critical cluster size of $N_S = 9 \pm 2$, a Hill coefficient (inverse cooperativity) of $\alpha = 0.21 \pm 0.12$, and a saturation force of $\langle \Delta F \rangle_{\max} = 1.3 \pm 0.2$ pN. No force increase was detected in dead clusters relative to single bacteria. Dashed regions indicate variability bands.

clusters within the trapping energy of a single optical tweezer ($N = 1$ to 20). Optical Tweezers in photon momentum mode (OT-PMM) measure the net force on the trapped cluster directly from momentum exchange, expressed as $\mathbf{F} = d\mathbf{p}/dt$ (43, 63). Cluster center-of-mass displacements correspond one-to-one with the punctual net force detected by OT-PMM, explicitly linking spatial tracking to force readout (*Materials and Methods*). Trapped cells exhibited in-plane diffusion under lateral forces, $\mathbf{F}(x, y) \equiv (F_x, F_y) = \mathbf{F}_0 + \delta\mathbf{F}$, where $\mathbf{F}_0$ represents the reaction force balancing the trap near the center-of-mass ($\mathbf{F}_0 = -\mathbf{F}_{trap} = k\mathbf{u}$; *SI Appendix*, Fig. S1 *A* and *B*). As shown in Fig. 2, both components align with the trapping z-beam's axis, ensuring $F_z = 0$ at the focal plane ($z = 0$) (44). Bacterial clusters were assembled by capturing single cells with a "fishing" tweezer and transferring them into a sensing trap (Fig. 2*A*, *Left* panels), enabling direct-force measurements while minimizing photodamage (*Materials and Methods*). Each cluster maintained a fixed number of viable, motile bacteria (N), behaving as a cohesive, mobile entity (Fig. 1 and Movie S1). Cluster sizes, $d(N)$, were visually assessed, ranging from single-cell size, $d_0 = 1.0 \pm 0.1$ μm ($N = 1$), up to $d_{\max} \approx 4$ μm for the largest clusters ($N \approx 20$) (*SI Appendix*, Fig. S1*C*). OT-PMM was performed under stable trapping conditions, with stiffness increasing linearly with cluster size, $k = 16 \rightarrow 20$ pN/μm (*SI Appendix*, Fig. S1 *D* and *E*). To define the energetic boundary conditions, we calibrated the trap's force–displacement profile (*SI Appendix*, Fig. S2), whose integration yields the effective three-dimensional "energy cup" confining bacterial motion (Fig. 1, *Upper* panels). Experiments were initiated after confirming stationary reciprocal force trapping ($\mathbf{F}_0 + \mathbf{F}_{trap} \Rightarrow$ zero offset) (43). Relevant fluctuating forces were directly recorded using OT-PMM, as $\delta\mathbf{F}_i \equiv (F_x, F_y)$, though they can be used to infer lateral displacements proportional to mobility impulses, $\Delta\mathbf{r}_i \equiv \mathbf{u}(x, y) \propto \delta\mathbf{F}_i/k$ (44). The fluctuating force components, $\delta\mathbf{F}(N)$, grew with cluster size N, while the mean trapping force remained approximately constant at $\mathbf{F}_0 \approx 0.5$ pN (*SI Appendix*, Fig. S3). Clusters were modeled as nonequilibrium steady-state (NESS) systems evolving in a coarse-grained phase space (CGPS), with active internal forces opposing external optical constraints (64). Control measurements using dead clusters and inert beads of similar size ($d \approx 1$ to 4 μm) confirmed that observed fluctuations were due to active motility (*SI Appendix*, Fig. S3). In the following, we analyze the cluster dynamics at the center-of-mass (CM) level along two complementary routes: first, by quantifying the instantaneous forces recorded by OT-PMM, and second, by examining the associated CM displacements obtained from MPT trajectories. These two views are mechanically equivalent and jointly define the energetic description of confined bacterial motion.

Stochastic Motility Forces of *P. mirabilis* Bacteria: From Individuals to Clusters. Fig. 2 compares the stochastic force behavior of single cells and clusters, for both living and dead states. Time-series of lateral forces $\delta\mathbf{F}_i$ under stationary trapping were analyzed through their variance, $\Delta F^2 = \langle \delta\mathbf{F}^2 \rangle = \langle F_x^2 + F_y^2 \rangle$, which provides a direct measure of motility strength under confinement. Living clusters showed markedly higher ΔF compared to isolated cells, alive or dead. The force distributions $P[F(N)]$ depend on motility state: Active clusters generate much stronger fluctuations than passive or dead cells ($\Delta F_{act} \approx 1.5$ pN vs. $\Delta F_{pass} \approx k_B T/\delta \approx 0.2$-0.3 pN, with $\delta \sim 10$ to 20 nm) (32, 33). These distributions follow Maxwell statistics, $P(\delta F) \propto \exp[-\Delta W(\delta F)/2\Delta F^2]$, where fluctuating work is $\Delta W = \delta F \Delta r \approx \delta F^2/k$ (*SI Appendix*, Fig. S4). Living clusters typically exhibited $\Delta F_{act} \approx 1.2$ to 1.5 pN, indicating nonequilibrium flagellar propulsion (27), while dead clusters remained near thermal equilibrium ($\Delta F_{pass} \approx \sqrt{k\, k_B T} \approx 0.2$ pN) (63). Fig. 2*B* demonstrates that active forces increase with cluster size N, starting at $\Delta F_0 = 0.28 \pm 0.12$ pN ($N = 1$) and saturating

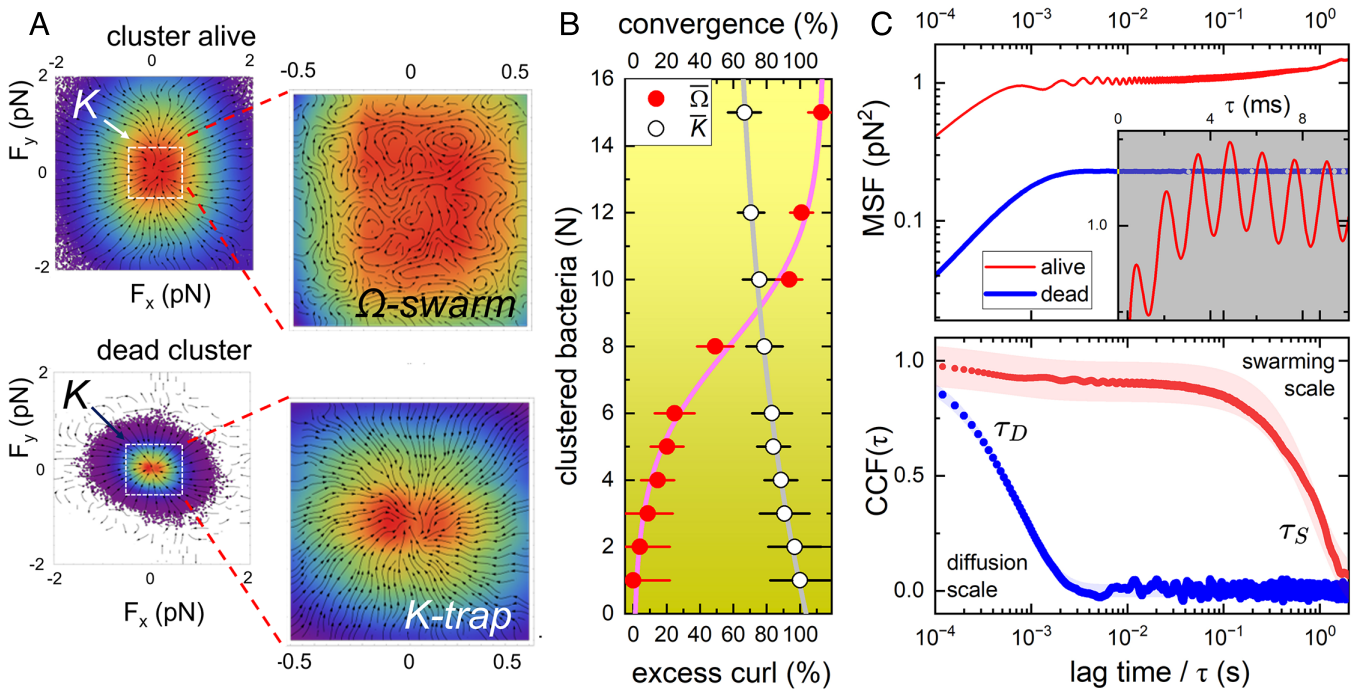

Fig. 3. CGPS fluctuating forces: (*A*) Collective force currents in living and dead clusters (*Left*). Zoomed-in views show the most populated regions at low forces (*Right*). In living clusters, swarming-broken detailed balance is seen as rotational Ω-currents preventing trap attraction (*Top*). In dead clusters, detailed balance appears as convergent currents toward central K-attractor (*Bottom*). (*B*) Force-field relative characteristics in living clusters: excess curl, $\bar{J}_\Omega \equiv (J_\Omega^{act} - J_\Omega^{pass})/J_\Omega^{act}$; relative convergence, $\bar{J}_K = J_K^{act}/J_K^{pass}$ (normalized means and bootstrapped SDs). (*C*) Force correlations over lag times: mean-square force impulses show short-time diffusivity followed by long-time confinement (*Top*); the rotatory flagellar mode appears at intermediate crossover times (*Inset*). Normalized cross-correlation functions (*Bottom*) reveal swarming activity at intermediate times ($\tau_D \le \tau \le \tau_S$), between rapid unconstrained diffusion (τ_D) and terminal swarm confinement relaxation (τ_S).

at $\Delta F_{act}^{(S)} \approx 1$ to 1.5 pN for $N \ge N_S \approx 10$. The force increase with cluster size follows a cooperative law, which we model using a Hill function (65):

$$\frac{\langle \Delta F \rangle}{\langle \Delta F \rangle_{\max}} = \frac{N^\alpha}{N_S^\alpha + N^\alpha}. \quad [1]$$

Here, α reflects initial steepness and N_S marks the swarm cooperative onset (Fig. 2*B*). Swarming criticality arises as $\langle \Delta F \rangle_{\max} \approx k_B T_{eff}(N_S)/\delta$, with $T_{eff}(N_S) > T$ (27). In contrast, passive clusters show no cooperative scaling and remain at Brownian fluctuation levels, consistent with thermal equilibrium at T (*SI Appendix*, Fig. S4).

Fluctuating Force Components: Coarse-Grained Phase-Space Decomposition. To evaluate motility efficiency in bacterial clusters, we examined whether active force correlations establish a mechanically consistent swarming mechanism within a coarse-grained phase space (CGPS) (27). By distinguishing correlated (nonthermal) from uncorrelated (thermal) fluctuations, we analyzed how dissipation in active swarms differs from that in inactive clusters diffusing in the optical tweezer's deformation-work space. This dynamic space is defined by in-plane forces $\mathbf{F}(x, y)$, driving overdamped displacements $\mathbf{u}(x, y) \propto \delta\mathbf{F}/k$ (*Materials and Methods*). Fig. 3 shows lateral fluctuating forces $\delta\mathbf{F} = (F_x, F_y)$, directly measured in CGPS under stationary probability, $dP(F_x, F_y)/dt = 0$ (11). The resulting NESS force currents, $\mathbf{J}_F = P(\delta\mathbf{F})\, d\mathbf{F}/dt$, describe stationary bacteromotive fluxes, linked to ensemble-averaged power injection, $\mathcal{P} = \int \mathbf{J}_F \cdot d\mathbf{u}$ (4, 41). In Fig. 3*A*, living clusters show scale-dependent flow fields (*Top*), contrasting with the purely overdamped motion of dead clusters (*Bottom*). At large displacements ($u \gg \delta$), trapping dominates ($F_{trap} \approx ku \approx 2$ pN), driving convergence to an equilibrium attractor $\mathbf{F}_K = 0$ at maximum probability $P_{\max}$ (*Left* panels). At small displacements ($u \approx \delta$), active swarms display vortex-like force fields ($\boldsymbol{\Omega}$), disrupting trapping convergence near $\mathbf{F}_K$ (Fig. 3*A*, *Top Right*). These vortices reach amplitudes of about 0.5 to 1 pN, larger than the local trapping forces (~0.2 pN), and generate spatial correlations consistent with NESS (28). Even a single motile bacterium disrupts the convergent flow seen in passive beads (*SI Appendix*, Fig. S6). These observations support a decomposition into conservative and dissipative forces, $\mathbf{F} = \mathbf{F}_{cons} + \mathbf{F}_{diss}$, interpreted as momentum fluxes within a Navier–Stokes (NS) framework (NS). Here, the propagation speed of hydrodynamic interaction is defined as $c \equiv k/\eta$, set by the ratio of trap stiffness k to internal viscosity η (*SI Appendix*, *Supplementary Note* N1).

Trapping Convergence and Active Vorticity: Broken Detailed Balance in Bacterial Swarms. The optical tweezer imposes a conservative force field, $\mathbf{F}_{cons} = -k\mathbf{u} = -\nabla U$, derived from the scalar potential $U_{trap} \approx \frac{k}{2}\mathbf{u} \cdot \mathbf{u}$, where $\mathbf{u}$ represents CGPS displacements. Dissipative contributions arise from frictional and swarming forces, $\mathbf{F}_{diss} = \mathbf{F}_{frict} + \mathbf{F}_S = \nabla \times \mathbf{A}$, with the generating vector potential $\mathbf{A} = \mathbf{F}_{\mathbf{frict}} \times \mathbf{u}$ capturing torque-like structured friction (*SI Appendix*, *Supplementary Note* N1). The viscous term, $\mathbf{F}_{frict} = -\hat{\boldsymbol{\zeta}}(t)\,\mathbf{v}$, depends on the anisotropic friction tensor $\hat{\boldsymbol{\zeta}}$, where diagonal terms reflect hydrostatic resistance and

off-diagonal terms encode directional coupling. This tensor may vary in time with active swarming forces, $\hat{\boldsymbol{\zeta}}[\mathbf{F}_S(t)]$, whose time derivative defines the curling tensor $\hat{\boldsymbol{\kappa}} = \partial\hat{\boldsymbol{\zeta}}/\partial t$. A negative determinant, $\det(\hat{\boldsymbol{\kappa}}) < 0$, signals lubrication driven by swarming forces. The Helmholtz–Hodge (HH) decomposition separates the force field into gradient and rotational components, $\mathbf{F} = \mathbf{F}_G + \mathbf{F}_R$, with $\mathbf{F_G} = -\nabla U_{trap} - \frac{1}{c}\partial_t\mathbf{A}$ and $\mathbf{F}_R = \nabla \times \mathbf{A}$. Here, $\partial_t\mathbf{A} = \mathbf{F}_S \times \mathbf{v}$ represents frictional dissipation, and $c = k/\eta$ is the propagation speed. These components underpin the NS-like dynamics of swarming:

A. Convergent flows arise from trap deformation ($\mathbf{F}_{trap} = -k\mathbf{u}$), and pressure gradients (∇p):

$$K = -\nabla \cdot \mathbf{F} = k + \nabla^2 p - \nabla \cdot \mathbf{F}_S \;\Rightarrow\; -\nabla \cdot \mathbf{F}_G, \qquad [2]$$

with $\mathbf{F}_S^{\parallel} = +\boldsymbol{\kappa}_{ij}\mathbf{u}$, and conservation enforced by the Coulomb gauge, $\nabla \cdot \mathbf{A} = 0$.

B. Vortical currents emerge under incompressibility ($\nabla\cdot\mathbf{v} = 0$):

$$\boldsymbol{\Omega} = \nabla^2(\hat{\zeta}\,\boldsymbol{\omega}) + \nabla \times \mathbf{F}_S \;\Rightarrow\; \nabla \times \mathbf{F}_R, \qquad [3]$$

where $\boldsymbol{\omega} = \nabla \times \mathbf{v}$ is the angular velocity. Transverse swarming forces $\mathbf{F}_S^{\perp} = +\hat{\boldsymbol{\kappa}}_{ij}\mathbf{u}$ generate vorticity via anisotropic modulation, with coupling terms linking isotropic and deviatoric components (*SI Appendix*, *Supplementary Note* N1).

Therefore, swarming dynamics depend on $\hat{\boldsymbol{\zeta}}(\mathbf{F}_S;\eta)$ and $\hat{\boldsymbol{\kappa}}(\mathbf{F}_S;\eta)$, forming an adaptive balance between trapping convergence and lubricated circulation (Fig. 3*A*). Energy flows $\mathbf{J}(E)$ decompose into $\bar{\mathbf{J}}_K$ and $\bar{\mathbf{J}}_\Omega$, integrated as $\bar{K} = \|\nabla \cdot \mathbf{F}\|$ and $\bar{\Omega} = \|\nabla \times \mathbf{F}\|$ (*SI Appendix*, Fig. S7). Fig. 3*B* shows the experimental data: Single cells display dominant convergence ($\bar{K} \sim 95$ to 100%, $\bar{\Omega} \approx 0$), whereas swarming clusters ($N \geq 9$ to 10) invert this balance, with vortical currents taking over. The addition of Dextran increased frictional currents with viscosity (*SI Appendix*, Fig. S8), confirming that detailed balance is broken under active dissipation, where $\mathbf{F}_{diss} \gg \mathbf{F}_{cons}$ (11). Swarm inactivation restored overdamped equilibrium ($\bar{\mathbf{J}}_\Omega = 0$), confirming that lubricated vorticity is a metabolically active, not passive, process (Fig. 3*A*, *Bottom*).

Force-to-Force Time Correlations: Fast Diffusion and Slow Swarming. We analyzed force time-series to identify causal correlations in bacterial clusters. Fig. 3*C* shows the mean-squared force fluctuations, $MSF(\tau) \equiv \langle[\mathbf{F}(t+\tau) - \mathbf{F}(t)]^2\rangle$, across lag times τ. At short timescales ($\tau \leq \tau_D \approx 1$ ms), the *MSF* grows linearly, $MSF_{diff}(\tau) \approx \Delta F_0^2(\tau/\tau_D)$, driven by thermal impulses with $\Delta F_0 \approx k_B T/\delta$ and $\delta \approx 10$ nm. Beyond this regime ($\tau \gg \tau_D$), a plateau emerges, $MSF_{conf} \approx \Delta F_{eff}^2$, representing confined fluctuations, where $\Delta F_{eff}^2 \approx (k_B T_{eff})k$ and $T_{eff} \geq T$ for $k \approx 20$ pN/μm (7, 11). Living clusters showed fluctuations more than an order of magnitude larger than dead cells, consistent with active propulsion, effectively corresponding to $T_{act} \sim 10T$. Notably, oscillatory features appeared near the crossover time ($\tau_{cross} \approx 10\tau_D$), revealing flagellar beating at $\omega_R \approx 360$ Hz (32, 33). The amplitude of these correlated impulses (~1 pN) is consistent with the scale of individual flagellar power strokes (31–33), establishing a direct quantitative link between the measured mesoscale fluctuations and underlying flagellar activity. Force relaxation was further characterized by the normalized cross-correlation function, $\overline{CCF}(F_x, F_y;\tau) \equiv [\langle F_x(t)F_x(t+\tau)\rangle + \langle F_y(t)F_y(t+\tau)\rangle - 2\langle F_x(t)F_y(t+\tau)\rangle]/2\Delta F^2$ (Fig. 3*D*). For inactivated cells, this correlation decayed as a single exponential, $\overline{CCF}_{pass}(\tau) \sim \exp(-\tau/\tau_D)$ with $\tau_D = 0.73 \pm 0.04$ ms, consistent with thermal motion ($D_0 \equiv \delta^2/2\tau_0$), where $\delta \approx 10$ nm ($\Leftarrow k_B T/F_0$). At this microscopic scale, diffusivity matched the passive elastohydrodynamic response speed, $c = k/\eta \approx 400$ μm/s ($\approx \delta/\tau_0$), assuming an effective internal viscosity $\eta \approx 50$ mPa · s (61). In contrast, living clusters displayed two distinct relaxation timescales: a fast component ($\tau_D = 0.3 \pm 0.2$ ms, ~10% amplitude) and a dominant slow swarming mode ($\tau_S = 0.6 \pm 0.2$ s, ~90% amplitude). Thus, force correlations in CGPS reveal a transition from rapid Brownian fluctuations to slower coordinated swarming.

In-Trap Bacterial Displacements by Multiple Particle Tracking: Cooperative Curling. Kinematic differences between living and dead bacterial clusters were assessed via real-space trajectories in optical traps (Fig. 1). Fast videomicroscopy with Multiple Particle Tracking (MPT) (53) allowed noninvasive estimation of velocities as $\dot{\mathbf{r}}(t) = \Delta\mathbf{r}/\Delta t$ from optical density variations (Movie S1). Center-of-mass trajectories, recorded as planar paths $\mathbf{r}(t) = (x, y)$, appeared directional and persistent in swarming clusters, but random and diffusive in dead ones (*SI Appendix*, Fig. S9). Real-space displacements, expressed in polar coordinates $\boldsymbol{\epsilon}_i = (\Delta r_i, \Delta\theta_i)$ relative to the trap center, were independently measured. Fig. 4*A* displays time-series of radial displacements, with living swarms showing oscillatory active motion (*Upper* panels) and dead clusters showing only passive fluctuations (*Lower* panels). Swarms oscillated at subsecond frequencies (3 to 4 cycles/s; $\omega_S \approx 20\ s^{-1}$) and exhibited preferred angular displacements, yielding non-Gaussian orientation distributions, unlike the symmetric Gaussians of dead clusters (*SI Appendix*, Fig. S10). These oscillations matched the slow collective relaxation time in CGPS force correlations (τ_S), with $\omega_S \gtrsim 2\pi/\tau_S$ (Fig. 3*D*). The much slower collective frequency ω_S compared to intrinsic flagellar rotation ($\omega_R \approx 10^3\ s^{-1}$; Fig. 3*C*, *Inset*) highlights emergent mesoscopic behavior rather than individual motor dynamics. This NESS-like motility reflects coupling between swarming forces and confinement relaxation (28). Fig. 4*B* shows polar displacement trajectories $\boldsymbol{\epsilon}(t) = [\Delta r(t), \Delta\theta(t)]$ exhibiting alternating pivot-like oscillations with angular gain $\Upsilon_S = \dot{\theta}/\dot{r} \approx 0.2$ mrad/nm, consistent with a confined "*tug-of-war*" between swarming directions ($\pm\Upsilon_S$). This antisymmetric motion reveals rotational structure, contributing directly to CGPS vorticity (*SI Appendix*, *Supplementary Note* N2). Thus, swarms maintain nonzero vorticity (Fig. 4*A*, *Left* panel), unlike isotropic, nonvortical dead clusters (*Right* panel).

Diffusive Mean-Square Displacements (MSDs): Swarming Oscillatory Correlations. We analyzed mean-squared displacements (MSD) computed over lag times as $MSD(\tau) = \langle[\mathbf{r}(t+\tau) - \mathbf{r}(t)]^2\rangle$ (*Materials and Methods*). Fig. 4*C* compares living swarms with dead clusters, both showing confined diffusivity consistent with an Ornstein–Uhlenbeck process in 2D, $MSD(\tau) \approx 4D(\tau)\,\tau_{\text{conf}}\left(1 - e^{-\tau/\tau_{\text{conf}}}\right)$. The apparent diffusion coefficient is given by $D(\tau) = D_{\text{eff}}^{(0)} + \Delta D_S(\tau)$, where $D_{\text{eff}}^{(0)} = k_B T_{\text{eff}}/\zeta_0$ represents an effective Einsteinian term (with ζ_0 as isotropic solvent friction), and $\Delta D_S(\tau)$ accounts for active swarming contributions (11, 62). The confinement time, $\tau_{\text{conf}} = \zeta_0/k$, depends on trapping stiffness k and solvent friction ($\zeta_0 \approx 6\pi d\eta_0$, with d the cluster size). We observed $\tau_{\text{conf}} \approx 0.5$–$1$ s (Fig. 4*C*), consistent with $k \approx 20$ pN/μm and $\zeta_0 \approx 2 \times 10^{-5}$ kg/s (61).

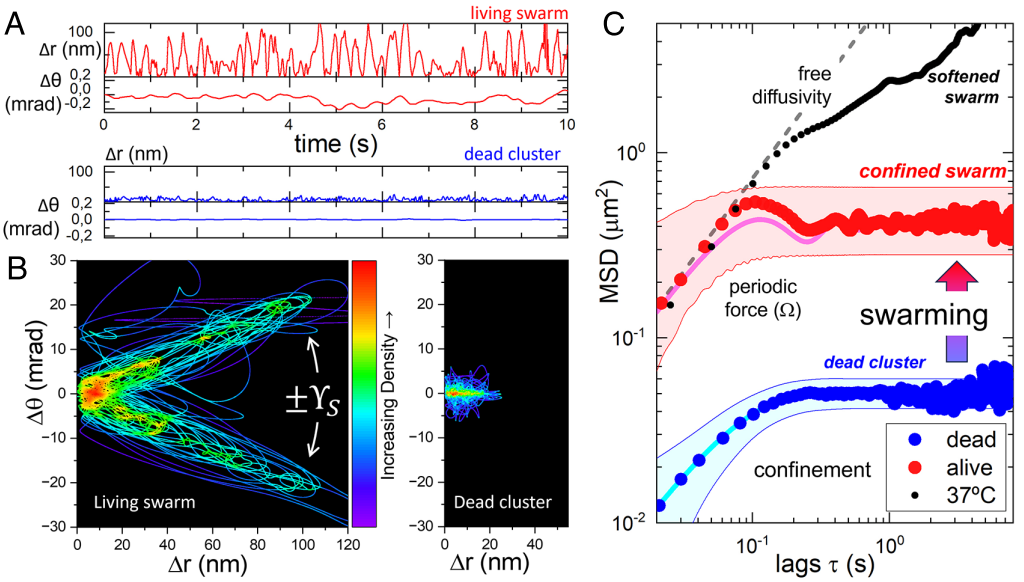

Fig. 4. Real-space cluster displacements in optical traps: (*A*) Patterns in polar displacements over time (distribution histograms; *SI Appendix*, Fig. S8). (*B*) Centre-of-mass' positions over time showing directed movements in a bacterial swarm maintained alive. The dead clusters undergo confined Brownian motion. (*C*) Mean square displacements: Dead (blue) and living clusters (red) at room temperature (22 °C). The dashed regions represent variability bands. Straight lines represents best fittings to confined diffusivity processes: overdamped Ornstein–Uhlenbeck in dead clusters (cyan); underdamped Brownian oscillator in living clusters (magenta); Einstenian free-diffusivity (gray); see main text for details. At physiological temperature (37 °C), living swarms develop longer displacements as an effective trap-softened hyperdiffusivity (black symbols).

At short times ($\tau \ll \tau_{\rm conf}$), $MSD \approx 4D_{\rm eff}^{(0)}\tau$, with bare diffusion $D_0 = k_BT/\zeta_0 \approx 0.05\,\mu{\rm m}^2/{\rm s}$. Dead clusters followed this thermal baseline ($D_{\rm pass}^{(0)} = 0.044 \pm 0.015\,\mu{\rm m}^2/{\rm s}$), whereas living swarms showed an order of magnitude higher diffusivity ($D_{\rm act}^{(0)} = 2.2 \pm 0.2\,\mu{\rm m}^2/{\rm s}$), indicating $T_{\rm eff} \gg T$. At long times ($\tau \gg \tau_{\rm conf}$), MSD plateaued at $4\sigma^2$, with $\sigma^2_{\rm pass} \approx 0.048\,\mu{\rm m}^2$ vs. $\sigma^2_{\rm act} = 0.45 \pm 0.12\,\mu{\rm m}^2$, giving $T_{\rm eff}/T \approx 9 \pm 2$ and a characteristic energy scale $\Delta E_{\rm act} \approx 10 k_BT$. Active swarming introduced an underdamped Brownian oscillator (62):

$$\Delta D_S(\tau) \approx \frac{\Delta E_{\rm act}}{\zeta}\sin^2(\omega_S\tau), \qquad [4]$$

with $\omega_S \approx 20\ {\rm s}^{-1}$ and diffusive strength $\sigma_S^2\omega_S \approx 0.5\,\mu{\rm m}^2/{\rm s}$. The resulting swarming speed $v_S \approx 100\,\mu{\rm m/s}$ remains below the elastohydrodynamic propagation speed $c \approx 400\,\mu{\rm m/s}$. This oscillatory process occurred over mesoscopic distances ($\sigma_S \approx 150$ nm $\gg \delta$) and much longer times than diffusive flights ($\tau_S \geq 50$ ms $\gg \tau_D$) (Fig. 1). As shown in Fig. 4*C* (*Upper* panel; softened swarm case), raising the temperature to physiological levels (37 °C) reduced confinement, leading to larger swarming displacements and longer relaxation times ($\tau_S \geq \tau_{\rm conf}$, $\sigma_{act} > \sigma_S \gg \sigma_{pass}$). Glucose enrichment further amplified activity, breaking detailed balance as reflected in CGPS changes (*SI Appendix*, Fig. S11).

Swarming Bursts: Active Diffusion Space. We characterized energy currents by quantifying motility work along trajectories: $d\bar{W}(\mathbf{F}, d\mathbf{r}) = \bar{\mathbf{F}}_i \cdot (\mathbf{r}_{i+1} - \mathbf{r}_i)$, using discrete Stratonovich multiplication, where $\bar{\mathbf{F}}_i = \{F_x, F_y\}$ denotes the mean fluctuating force during $\Delta t = [t_i, t_{i+1}]$, and $\mathbf{r}_i = \{x, y\}$ is the center-of-mass position (4, 16). Fig. 5*A* shows that active clusters produce bursts lasting $\tau_S \approx$ (200 to 600) ms with work amplitudes from a few to several tens of k_BT, clearly exceeding equilibrium values $\langle d\bar{W}_{eq}\rangle \approx k_BT$. Rotational work was defined as $d\bar{W}_R = \bar{\mathbf{T}}_i \cdot \Delta\theta_i$, with torque $\bar{\mathbf{T}}_i = \bar{\mathbf{F}}_i \times \mathbf{r}_i = (0, 0, \bar{T}_z)$, where $\bar{T}_z = \bar{F}_x\Delta y - \bar{F}_y\Delta x$. Active swarms exhibited rotational contributions ($d\bar{W}_R \geq k_BT$), while dead clusters remained near zero (Fig. 5*A*, *Bottom*). As shown in Fig. 5*B*, translational bursts were driven by swarming forces ($\Delta E_{act} \approx 10 k_BT$), with a secondary torque component $d\bar{W}_R \approx \Delta E_{act}\Upsilon_S(d/2) \approx k_B(T_{\rm eff} - T)$ reflecting vorticity (*SI Appendix*, *Supplementary Note* N2). Passive clusters showed neither translational nor rotational bursts (Fig. 5*B*, *Inset*). These observations align with a structured NS-framework (*SI Appendix*, *Supplementary Note* N1), where NESS swarming emerges from: *i)* translational convection: $W - W_{\rm trap} \approx \hat{\zeta}_{ii}(t)D_{\rm eff} \approx k_BT_{\rm eff} \Rightarrow \nabla \cdot F_S \approx K - k$, and *ii)* rotational vorticity: $W_R \approx \hat{\zeta}_{ij}(t)\Delta D_S \approx k_B(T_{\rm eff} - T) \Rightarrow \nabla \times F_S \propto \Omega$ (Eqs. **2** and **3**). Both occur under thermal fluctuations satisfying $\zeta_0 D^{(0)} \approx k_BT \propto \nabla^2 p$ (49). Together, isotropic divergent bursts and anisotropic vortical curling support the oscillatory flagellar *tug-of-war* (Figs. 3 and 4), governed by structured time-dependent friction $\hat{\boldsymbol{\zeta}}(t)$ and lubricated active forces $\mathbf{F}_S(\hat{\boldsymbol{\kappa}}) = +\hat{\boldsymbol{\kappa}}\,\mathbf{u}$, in contrast with passive isotropic diffusion ($\hat{\boldsymbol{\kappa}}_{\rm pass} \equiv 0$). Most swarming events occurred within a single oscillatory half-cycle, exceeding the activation threshold for unconfined motion (Fig. 5*B*).

Cumulative Trapping Work: Frictional Gauges. To quantify how confined bacteria use energy, we measured their cumulative work against the optical trap, distinguishing conservative trapping from dissipative swarming. We analyzed center-of-mass trajectories $\Gamma[\mathbf{r}_i(t_i)] = (x_i, y_i)$ and computed cumulative motility work using the Stratonovich integral (4):

$$\bar{W}[\Gamma(t)] = \int_0^t d\bar{W}(t) \approx \sum_i \bar{\mathbf{F}}_i \cdot \Delta\boldsymbol{r}_i, \qquad [5]$$

where $\bar{\mathbf{F}}_i$ is the mean fluctuating force over $\Delta t = [t_i, t_{i+1}]$, and $\Delta\mathbf{r}_i$ the corresponding displacement.

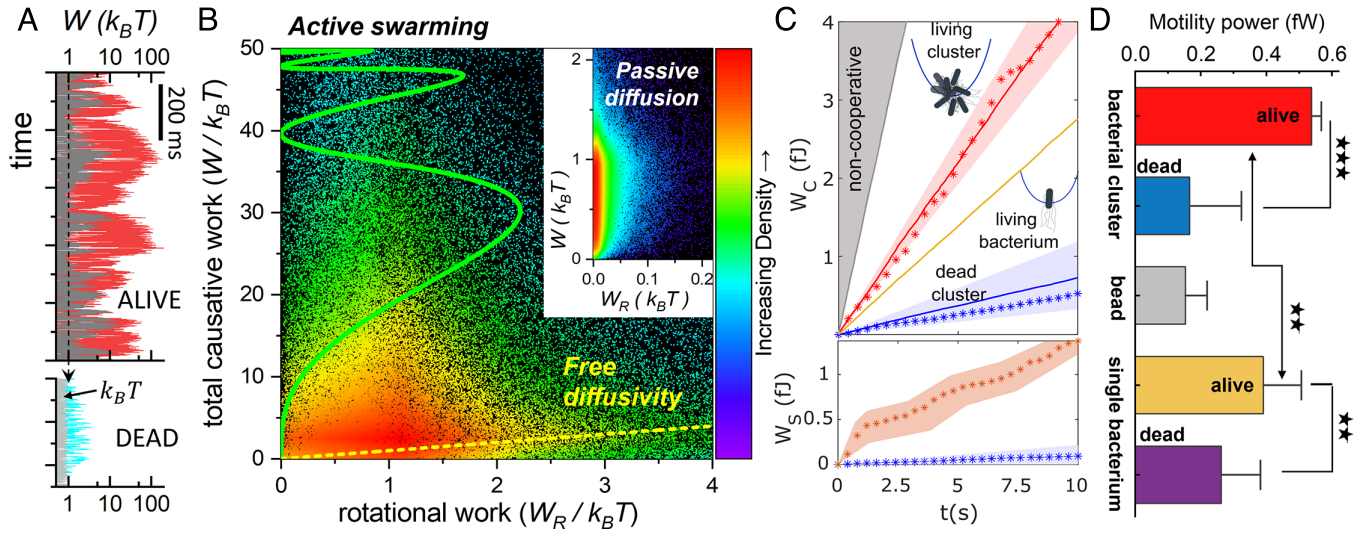

Fig. 5. Swarming energetics measured from *P. mirabilis* clusters' center-of-mass motion. (*A*) Experimental time series of work increments in bacterial clusters: live swarms (*Top*) and dead clusters (*Bottom*). Bursts of causative motility work (W, red) emerge with the presence of rotational energy W_R (gray). (*B*) Energy CGPS for motility work: probability currents flow from high rotational work (W_R), driving increased total motility work depending on confined active diffusivity after lag time, $W[W_R, D(\tau)]$. Diffusive trajectories in parametric time: active swarming $W_R = \zeta\,\Delta E_{\rm act}\,\sin^2(\omega_S\tau)$ and $W = \zeta\,[D^0 + \Delta D_S(\tau; \Delta E_{\rm act}, \omega_S)]$ (green line: $\Delta E_{\rm act} = 20\,k_BT$ and $\omega_S = 20\,{\rm s}^{-1}$); passive free diffusivity $W = W_R = \zeta\,D^{(0)}$ (yellow dashed line). (*C*) Cumulative work as a function of integration time (*Top*): path-independent (dots) vs. path-dependent (lines), for live clusters (red) and dead clusters (blue). Straight lines represent best fits to Ohm-like currents. (*Bottom*) Rotational work emerges as the swarming force imposes an Ohmic linear current; same symbols apply. (*D*) Effective power inferred from velocity fluctuations and force–current persistence under microconfined dissipation. The motility power $\mathcal{P}$, defined as the rate of change of total mechanical energy, was calculated from W–t slopes in panel (*C*) (see main text for details). This measure does not represent the total metabolic heat released by the bacteria, but rather a velocity-resolved, coarse-grained proxy for entropy production through motility power, capturing the energetic cost of synchronizing microscopic fluctuations into coherent flows.

Alternatively, from the trap's Hookean relation $\mathbf{F}_{trap} = -k\Delta\mathbf{r}$, displacements were inferred as $\mathbf{dr}_i \Leftarrow \mathbf{F}_i/k$ (43). This provides a path-independent proxy for cumulative work:

$$\bar{W}_{\rm inf}(t) \approx \frac{1}{k}\sum_i \left(F_{x_i}^2 + F_{y_i}^2\right). \qquad [6]$$

Notably, the two complementary routes of displacement estimation, either direct from MPT trajectories or inferred from OT-PMM forces proved fully consistent, jointly validating the center-of-mass energetic description. Fig. 5*C* shows ensemble averages ($N \approx 20$ cells per cluster, > 50 realizations) confirming $\bar{W} \approx \bar{W}_{\rm inf}$, with the decomposition $\bar{W} = \bar{W}_{cons} - \bar{W}_{diss}$ holding within experimental uncertainty for both active and passive systems. Here, $\bar{W}_{cons}$ denotes conservative trap work, while $\bar{W}_{diss}$ quantifies dissipative work against it (7, 16). Energy transport is governed by all of them, trapping confinement ($\mathbf{F}_{\rm trap} = -k\,\mathbf{u}$), viscous drag ($\mathbf{F}_{\rm frict} = -\hat{\boldsymbol{\zeta}}\,\mathbf{v}$), and swarming propulsion ($\mathbf{F}_S = +\hat{\boldsymbol{\kappa}}\,\mathbf{u}$), with $\mathbf{v} = d\mathbf{u}/dt$ the dissipative velocity (*SI Appendix, Supplementary Note* N3). The energy loss rate is captured by the Rayleigh dissipation function (66):

$$\Phi(\mathbf{F}_{\rm diss}) = \frac{dW_{\rm diss}}{dt} = \frac{1}{2}\int \mathbf{F}_{\rm diss}\cdot d\mathbf{v}, \quad \mathbf{F}_{\rm diss} = \mathbf{F}_{\rm frict} + \mathbf{F}_S, \quad [7]$$

yielding the ensemble-averaged power:

$$\mathcal{P} = \left\langle \frac{dW}{dt} \right\rangle = \bar{K}_{\rm cons} - \bar{\Phi}_{\rm diss}, \qquad [8]$$

where $\bar{K}_{\rm cons} = c\,\langle \mathbf{F}_{\rm trap}\rangle$ is the conservative input (with $c = k/\eta$ as the elastohydrodynamic rate), and $\bar{\Phi}_{\rm diss}$ the total dissipation.

In passive clusters, confinement is opposed only by isotropic friction, $\hat{\boldsymbol{\zeta}}_{\rm pass} = \zeta_{\rm iso}\mathbf{I}$, giving $\bar{\Phi}_{\rm diss} \approx \bar{\Phi}^{\rm (pass)}_{\rm frict}$ and ensuring equilibrium between trap work and frictional losses (blue symbols, Fig. 5*C*). By contrast, active clusters show time-dependent deviatoric friction,

$$\hat{\boldsymbol{\zeta}}_{\rm act}(t) \approx \hat{\boldsymbol{\zeta}}_{\rm pass} - \hat{\boldsymbol{\kappa}}\,t, \qquad [9]$$

where the swarming gauge $\partial_t\mathbf{A} = \mathbf{F}_S \times \mathbf{v}$ enters via lubricated curling ($\hat{\boldsymbol{\kappa}}$).

The active power budget thus reads

$$\mathcal{P}_{\rm act} = \bar{K}_{\rm cons} - \bar{\Phi}^{\rm (act)}_{\rm frict} + \bar{\Phi}_S, \qquad [10]$$

exceeding $\mathcal{P}_{\rm pass}$ due to swarming gains minus effective frictional losses (Fig. 5*C*). Thus, energy balance follows as

$$\mathcal{P}_{\rm act} = \mathcal{P}_{\rm pass} + \bar{\Phi}_S(\bar{\zeta}) - \bar{\Phi}_L(\bar{\kappa}), \qquad [11]$$

where $\bar{\Phi}_L \equiv \bar{\Phi}^{(pass)}_{frict} - \bar{\Phi}^{(act)}_{frict} \propto \bar{\kappa}\,\bar{v}^2$ is the lubrication gauge (active input from curling, $\bar{\kappa} = \langle \int \kappa_{ij}(t')dt' \rangle$), and $\bar{\Phi}_S = \langle \mathbf{F}_S \cdot d\mathbf{v}\rangle \propto R\,\bar{v}^2$ the swarming gauge (with resistance $R = \langle \det(\zeta_{ij})\rangle$) (*SI Appendix, Supplementary Note* N4).

Hence, the average normal gauge potential,

$$\langle \partial_t \mathbf{A}_z \rangle = \langle \mathbf{F}_S \times \mathbf{v}\rangle_z = \bar{\Phi}_S - \bar{\Phi}_L = \mathcal{P}_{act} - \mathcal{P}_{pass} > 0, \qquad [12]$$

captures net energy flow sustained by deviatoric friction. Since $\bar{\Phi}_S$ arises solely from anisotropic (curling) components, it excludes convergent flows in $\bar{\Phi}_L$. Together, $\bar{\Phi}_S$ and $\bar{\Phi}_L$ define the anisotropic energy balance of swarming under confinement (*SI Appendix, Supplementary Note* N4).

Dissipated Motility Power: Ohmic Currents. To quantify the energetic cost of sustaining cooperative vortices (39), we expressed

the dissipated power of swarming activity in a simple Ohmic form, analogous to Joule heating (64, 66):

$$\mathcal{P}_{\text{act}} = R_\zeta \bar{J}_\Omega^2, \quad [13]$$

where $R_\zeta = \langle \hat{\zeta}(\eta, \mathbf{F}_{\text{diss}}) \rangle$ is the effective friction coefficient, and $\bar{J}_\Omega$ the coarse-grained rotational (vortical) dissipation current generated by swarming-induced curl (*SI Appendix*, *Supplementary Note* N5). The convergent component $\bar{J}_K$ does not contribute, being absorbed by passive frictional dissipation. This Ohmic current also satisfies the first Joule's law (Fig. 5*C*):

$$\bar{W}_{\text{diss}}(t) = \bar{\Phi}_{\text{diss}}\, t \approx R_\zeta \bar{J}_\Omega^2\, t, \quad [14]$$

with effective resistance estimated as $R_\zeta \approx \bar{V}_S/\bar{J}_\Omega$, where $\bar{V}_S(\bar{F}_S, \bar{K}_{\text{cons}})$ is the mean swarming potential set by optical confinement. Experimentally, this resistance scales linearly with medium viscosity ($R_\zeta \propto \eta$), as verified by adding Dextran (*SI Appendix*, Fig. S8). Since Dextran raises η without affecting intrinsic motility forces F_S, this isolates viscous damping as the sole source of increased dissipation (*SI Appendix*, Fig. S12*A*). With $\bar{V}_S$ held constant, cumulative trap work decreases with viscosity ($\bar{K}_{\text{cons}} \propto k/\eta$, *SI Appendix*, Fig. S12*B*), while dissipated power increases inversely with resistance ($\bar{\Phi}_{\text{diss}} = \bar{V}_S^2/R_\zeta$, *SI Appendix*, Fig. S12*C*). Hence, the NS-dissipation rate defines differential Ohmic gauges, $\bar{\Phi}_{\text{diss}} = \bar{\Phi}_L - \bar{\Phi}_S$, reflecting how CGPS dissipative forces channel net vortical dissipation current through

$$\bar{J}_\Omega = \bar{V}_S/R_\zeta \quad \Leftarrow \quad \langle \mathbf{F}_{\text{diss}}(\zeta, \kappa) \times \mathbf{v} \rangle_\Omega > 0.$$

As a reference, the motility work of a single bacterium $\bar{W}_0^{(1)}$ lies between passive motion ($\bar{J}_\Omega = 0$) and collective swarming ($\bar{J}_\Omega \gg 0$) (Fig. 5*C*). The uncooperative bound, $\bar{W}_{\text{UC}} = N\bar{W}_0^{(1)} \gg \bar{W}$, highlights the efficiency of swarm-level force coordination. Finally, the observed path-independence of $\bar{W}$ under metabolism-fixed $\bar{V}_S$ confirms a steady Ohmic regime, where power is regulated by the interplay of frictional ($\bar{\Phi}_L$) and active ($\bar{\Phi}_S$) dissipation.

Swarming Work: Dissipative Vortices. Swarming-induced rotational work was quantified by the cumulative angular energy,

$$\bar{W}_R(t) = \int_0^t \mathbf{F}_S \cdot d\boldsymbol{\theta} \approx \sum_i (\mathbf{F}_i \times \mathbf{dr}_i) \cdot \hat{\mathbf{z}}, \quad [15]$$

which tracks the work performed by active forces along angular displacements in the trapping plane.

Fig. 5*C* (*Bottom*) shows that only living swarms generate significant rotational work, scaling as $\bar{W}_R \propto \bar{J}_\Omega^2\, \bar{\kappa}\, t$, while dead clusters remain inactive ($\bar{J}_\Omega^{(\text{pass})} = 0$). The associated dissipation, $\bar{\Phi}_\Omega = \frac{1}{2}\langle \mathbf{F}_{\text{diss}} \times \mathbf{v} \rangle_z$, arises from the interplay of swarming forces ($\mathbf{F}_S = +\hat{\boldsymbol{\kappa}}\mathbf{u}$) and structured friction ($\mathbf{F}_{\text{frict}} = -\hat{\boldsymbol{\zeta}}\mathbf{v}$). The Ohmic character of this power stroke, $\bar{\Phi}_\Omega \propto \bar{\Phi}_S - \bar{\Phi}_L$, links active lubrication to net energy loss through confined vortical motion (*SI Appendix*, *Supplementary Note* N4). In living *P. mirabilis* swarms, active angular displacements scale with vorticity upon frictional resistance:

$$\bar{W}_R \equiv \langle \mathbf{F}_S \times \mathbf{u} \rangle_z \approx T(\boldsymbol{\Omega})\, \Upsilon_S\, \Delta r \propto \frac{\boldsymbol{\Omega}^2}{2R_\zeta}, \quad [16]$$

where the normal torque $T(\boldsymbol{\Omega}) = (\nabla \times \mathbf{F}_S)_z$ captures swarming-induced circulation.

The observed rotational work identifies swarming vortices as dissipative, Ohmic-like currents driven by internal friction under active lubrication (*SI Appendix*, Fig. S13). Moreover, increased rotational work correlates with enhanced diffusivity, $\bar{W}[\bar{W}_R, \Delta D_S(\omega_S)]$ (Fig. 4), highlighting cooperative flagellar dynamics. These results support the existence of a critical swarm size $N \geq N_S$ at which mesoscale vortices emerge as collective energy states (Figs. 2 and 5*B*). Similar rotational enhancement has been observed in *Chlamydomonas*, where beat alignment boosts oscillatory power extraction (67).

Stochastic Energetics: Dissipated Power. Fig. 5*D* shows motility power calculated under different conditions. Living swarms operate at a rate of $\mathcal{P}_S = (1.3 \pm 0.2) \times 10^5\, k_B T/\text{s} \approx 0.52\,\text{fW}$, consistent with active diffusion estimates $\mathcal{P}_S \approx \Delta E_S/\tau_D$. By contrast, dead clusters move much less, $\mathcal{P}_{\text{dead}} \approx 3.2 \times 10^3\, k_B T/\text{s}$. For reference, the motility power of a single bacterium is $\mathcal{P}_1 \approx 0.34\,\text{fW}$, while an uncoordinated aggregate of $N = 10$ cells, $\mathcal{P}_{\text{UC}} = N\mathcal{P}_1 \approx 3.4\,\text{fW} \gg \mathcal{P}_S$. This inequality ($\mathcal{P}_S < \mathcal{P}_{\text{UC}}$) highlights a scaling law of cooperative efficiency: As swarms grow, their collective power increases sublinearly with cell number, reflecting redistribution of motile forces into coherent vortical flows rather than additive, uncorrelated losses. Thus, cooperative swarming realizes mesoscopic dissipation well below the uncooperative bound, underscoring its optimal efficiency in nonequilibrium steady states (NESS) through frictional cooperativity.

The dissipated power of bacterial swarming can be analyzed within the stochastic energetics framework of Shinkai and Togashi (49), which links effective diffusion to power dissipation under nonequilibrium conditions (2). In our system, the effective diffusion coefficient decomposes as $D_{\text{eff}}(\tau) = D^{(0)} + \Delta D_S(\tau)$, where $D^{(0)}$ represents thermal fluctuations at an effective temperature T_{eff}, and $\Delta D_S(\tau) = (\Delta E_S/\zeta)\sin^2(\omega_S \tau)$ is the active, time-dependent component consistent with underdamped swarming (Fig. 4). During the active diffusion window ($\tau \leq \omega_S^{-1}$), the cumulative motility work is given by $\bar{W}(\tau) = \int_0^\tau \mathbf{F} \cdot \mathbf{v}\, dt$, dissipated through viscous forces $\mathbf{F}_{\text{frict}} = -\hat{\boldsymbol{\zeta}}\mathbf{v}$ (Fig. 5*C*). The corresponding power dissipation, $-\bar{Q}(\tau) = \bar{W}(\tau) - 2k_B T$, accounts for frictional losses above the thermal baseline (49). Energy conservation requires $\Delta E = \bar{W}_{\text{frict}} + \bar{Q}$, from which the dissipation rate is defined as

$$\Delta\mathcal{P} = \mathcal{P}_{\text{act}} - \mathcal{P}_{\text{pass}} = \frac{d\bar{W}_{\text{frict}}}{dt} = -\frac{d\bar{Q}}{dt}, \quad [17]$$

providing a direct measure of irreversible energetic cost (41).

The corresponding entropy production rate is

$$\sigma = \frac{\Delta\mathcal{P}}{T} \geq 0, \quad [18]$$

which offers a thermodynamically consistent measure of dissipation, with $\Delta\mathcal{P} = \bar{\Phi}_S - \bar{\Phi}_L$ capturing the balance between active lubrication and frictional losses in vortical flows. The cooperative swarm yields an entropy production rate of $\sigma_S \approx (\mathcal{P}_S - \mathcal{P}_{pass})/T \approx 10^5\, k_B/\text{s}$.

Discussion

Our findings provide a mechanistic framework for understanding bacterial swarms as NESS regulated through collective power

flows. Using optical confinement and CGPS analysis, we resolve how conservative trapping forces interact with active, time-correlated fluctuations in living *P. mirabilis* clusters. Decomposing force fields into gradient and solenoidal components within an active Navier–Stokes (NS) framework reveals two complementary modes of power redistribution: conservative flows dominating passive response, and dissipative vortical currents arising from lubrication-mediated self-interaction during flagellar strokes. These NS modes are encoded in the effective friction tensor $\hat{\boldsymbol{\zeta}}(t)$, with a time-independent isotropic baseline ($\zeta_{ii} \propto \eta$) and a time-dependent deviatoric part reflecting lubrication stresses. Its time derivative, the curling tensor $\hat{\boldsymbol{\kappa}} \equiv \partial_t \hat{\boldsymbol{\zeta}}$, sustains vortical circulation driving operational dissipation. Motility follows Ohmic-like power, $\mathcal{P} = \bar{\zeta} v^2$, with an underlying rotational channel arising from lubricated vortices, $\mathcal{P}_R = \bar{\kappa}\Omega^2 \ll \mathcal{P}$. Despite trajectory complexity, cumulative dissipation is path-independent, indicating that once circulation emerges, energy loss is governed by the lubricated reorganization of frictional pathways. As shown in Fig. 6, swarming power in trapped clusters saturates at a cooperative plateau $\mathcal{P}_S \simeq 0.52\,\mathrm{fW}$, well below the uncoordinated bound $\mathcal{P}_{\mathrm{UC}} = N\mathcal{P}_1$ (Fig. 6*A*). For critical cluster sizes $N \gtrsim N_S \simeq$ 9-10, the rotational contribution reaches $\mathcal{P}_R \simeq 0.15\,\mathrm{fW}$. This rotational power is consistent with the composition of $N_S \simeq 10$ flagellar power strokes of amplitude $F_{\mathrm{flag}} \sim 1\,\mathrm{pN}$ acting over a lever arm $d \sim 4$ to $5\,\mu\mathrm{m}$, i.e. torques $T_{\mathrm{flag}} \sim F_{\mathrm{flag}} d \simeq 10^{-18}\,\mathrm{N\,m}$ that remain correlated over an effective cooperation time τ_{coop} lying between the fast diffusive time $\tau_D \simeq 1\,\mathrm{ms}$ and the slow swarming time $\tau_S \simeq 0.6\,\mathrm{s}$. A simple scaling $\mathcal{P}_R \sim N_S T_{\mathrm{flag}}/\tau_{\mathrm{coop}}$ then yields $\mathcal{P}_R \sim 10^{-16}$ to $10^{-15}\,\mathrm{W}$ ($\approx$0.1 to 1 fW), consistent with the measured $\mathcal{P}_R \simeq 0.15\,\mathrm{fW}$ (Fig. 6*A*). The onset of cooperativity reflects thus a symmetry-breaking transition of the friction tensor, where isotropic convergent relaxation is replaced by lubricated rotational channels sustaining persistent vortices. Indeed, the parametric plot shows that vortex-dominated swarms ($N \geq N_S$) collapse onto a narrow branch of nearly constant total power (Fig. 6*B*), indicating that the cooperative plateau is set by rotational lubrication rather than by increased metabolic input. ATP hydrolysis provides $\Delta G^{\circ}_{\mathrm{ATP}} \simeq -30.5\,\mathrm{kJ/mol}$ ($\approx$13 $k_{\mathrm{B}}T$ per molecule), of which $\sim$4 $k_{\mathrm{B}}T$ is dissipated as entropy (31). For intracellular ATP concentrations of 1 to 10 mM in a cell volume of $\sim$1 fL, the free-energy reservoir per cell is $E_{\mathrm{ATP}} \sim 10$ to 100 fJ, so over the swarming correlation time $\tau_S \approx 0.6\,\mathrm{s}$ a swarm of $N_S \sim 10$ cells releases $\mathcal{P}_M^{\mathrm{swarm}} \sim 0.2$ to 2 pW, mostly as heat. In contrast, our CGPS analysis isolates the mesoscopic swarming contribution as the entropy production of vortical currents, $\Delta\mathcal{P}_S \sim 0.5\,\mathrm{fW}$ i.e., $\sim 10^{-3}$ of total picowatt power. Thus, lubricated vortices channel only a minute fraction of the available power into coherent motion, leaving most of the energy for core cellular functions.

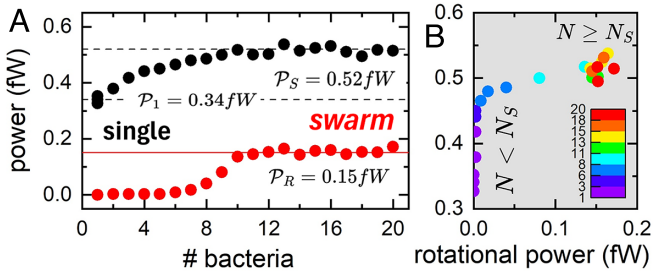

Fig. 6. Cooperative scaling of motility power in confined *P. mirabilis* clusters. (*A*) Motility power as a function of the number of bacteria in the trapped cluster. Black symbols: total power $\mathcal{P}(N)$ from the slope of cumulative work–time curves. Dashed lines indicate the single-cell bound ($\mathcal{P}_1$) and the cooperative plateau ($\mathcal{P}_S$). Red symbols: rotational contribution $\mathcal{P}_R(N)$, approaching $\mathcal{P}_R \simeq 0.15\,\mathrm{fW}$ in the swarming regime. "Single" and "swarm" denote, respectively, the low-*N* single-bacterium–like and high-*N* cooperative regimes. (*B*) Parametric plot of total power vs. rotational power, color-coded by cluster size *N*. The transition at $N \approx N_S$ separates a low-power regime ($N < N_S$) from a vortex-dominated cooperative regime ($N \geq N_S$), where rotational lubrication channels activate swarming work.

From a stochastic thermodynamic perspective (5–7), this disparity shows how living systems redistribute fluctuations through near-optimal channels of dissipation. According to the Jarzynski equality, all stochastic trajectories contribute to the free-energy balance, but those minimizing excess work dominate; in the low-velocity Ohmic regime, where $W_{\mathrm{diss}} \simeq \int v\hat{\zeta}\, v\, dt \sim \Delta\mathcal{P}_S t$, they align with the minimal eigenmodes of the effective friction tensor. Our results indicate that swarms exploit precisely these low-resistance, lubricated pathways, routing fluctuations into Jarzynski-optimal thermodynamic channels. For the cooperative plateau, $\Delta\mathcal{P}_S \simeq 0.5\,\mathrm{fW}$ corresponds to an entropy production rate $\sigma_S = \Delta\mathcal{P}_S/T \approx 10^5\, k_{\mathrm{B}}\,\mathrm{s}^{-1}$, comparable to reported values for highly motile biological systems (15, 41). This mesoscale view complements the biomolecular picture of Foster et al. (23) and the higher-scale cellular view of Di Terlizzi et al. (15), where only a small fraction of total dissipation flows through organized currents. Simple analysis within the Shinkai-Togashi framework (49) has shown how motility-induced work balances dissipate power with strictly positive, but relatively small entropy production, supporting the interpretation of swarms as adaptive NESS systems that optimize motility through lubricated vortices.

In summary, our findings identify lubricated vortical dissipation as the key control parameter of swarming cooperativity, linking deformation, force transmission, and energetic efficiency in confined bacterial collectives. Taken together, they establish optically trapped clusters as reductionist models of swarming that do not reproduce colony-scale spreading, but isolate minimal cooperative units-synchronized flagellar strokes, lubrication stresses, and vortical currents that underpin swarming mechanics. By quantitatively linking nanometric impulses to mesoscale circulation, our framework bridges single-cell energetics with collective transport strategies and situates optical confinement as a mechanistic complement to ecological assays. Finally, because cooperativity can be perturbed via controlled mechanical (trap stiffness, oscillatory confinement) or biological interventions (flagellar mutants, quorum-sensing, or metabolic inhibitors), these bacterial clusters offer a versatile platform to dissect the mechanisms of collective swarm dissipation.

Conclusion and Outlook

This study establishes a quantitative mechanical link between bacterial swarming and nonequilibrium thermodynamics by using stochastic energetics to resolve energy flows in confined *P. mirabilis* clusters. Combining photon momentum optical tweezers with multiple-particle tracking, we directly measured motility power dissipation and showed that trapped swarms behave as cooperative nonequilibrium steady states (NESS), where metabolic energy is redistributed between convergent trapping and lubricated rotational currents that break detailed balance and sustain persistent motility beyond thermal limits.

A central thermodynamic insight is that swarms achieve mechanical cooperativity by channeling only a minute fraction of their picowatt metabolic budget into coherent rotational motion, concentrating entropy production $\sigma_S \sim 10^5 k_{\mathrm{B}}/s$

in mesoscale vortices. Within the framework of fluctuation theorems, this efficiency reflects Jarzynski-optimal trajectories that minimize excess work by aligning motion along low-resistance, lubricated eigenmodes of the effective friction tensor. Cooperative dynamics thus emerges from adaptive flagellar coordination regulated by structured active stress and friction, providing a thermodynamically tuned mechanism for collective transport at minimal energetic cost.

Optically confined clusters therefore function as reductionist models of swarming, isolating minimal cooperative units-synchronized flagellar strokes, lubrication stresses, and vortical currents, while remaining amenable to controlled mechanical and biological perturbations. This framework offers a general route to quantify motility power and entropy production in active matter and can be extended to macroscopic colony phenomena such as surface swarming and biofilm formation, as well as to eukaryotic cell collectives, to explore how living matter exploits optimal thermodynamic pathways to channel metabolic energy efficiently across scales.

Materials and Methods

Bacterial Samples. We used *P. mirabilis* due to its high swarming motility (60). This rod-shaped bacterium, bearing 4-10 flagella, reaches swimming speeds up to 20 μm/s in optimal liquid media (57, 58). Cultures were grown in LB medium, refreshed biweekly, and maintained at 4 °C. For experiments, cells were incubated at 37 °C for 24 h. Nonmotile, dead bacteria were prepared by glutaraldehyde fixation (2.5%), followed by centrifugation and resuspension in PBS (52). Experiments were performed using 20 μL of suspension in sealed chambers (1 cm^2 area, 1 mm thick cover glass).

Optical Tweezers. We employed a multitrap optical tweezers (OT) platform (SensoCell, Impetux Optics S.L., Spain) based on photon momentum detection (PMM) (43). The setup uses a 1,064 nm NIR laser (1 W at objective, 23 mW at sample), with acousto-optic beam steering and a 60× water-immersion objective (NA 1.2). In PMM, optical forces are obtained directly from the momentum change of scattered light, yielding absolute in-plane force measurements, $\mathbf{F}(x, y) = d\mathbf{p}/dt$ (42). At equilibrium, the axial force vanishes at the trap plane ($F_z = 0$). Single traps induced cluster formation at cell concentrations of 10 to 20 per field. The system was temperature-stabilized using a Peltier module. A CMOS camera (Thorlabs) enabled sample imaging, and high-frequency force readouts (14 kHz) were digitized via a position-sensitive detector and controlled through LabVIEW. PMM thus provides direct, calibration-free measurements of the net force acting on each trapped cluster as a whole, ideally suited for probing bacterial motility (41, 44).

Trap Stiffness. Trap stiffness was determined via the "Particle Scan" protocol in SensoCell software (43). Forces were related to detector voltages as $\mathbf{F}(x, y, t) = \hat{\alpha} V(t)$, with $\hat{\alpha}(x, y)$ a transfer function (44). Total forces were decomposed into static ($\mathbf{F}_0 = \hat{\alpha} V_0$) and fluctuating components ($\delta\mathbf{F} = \hat{\alpha}\Delta V$). Force time-series were recorded at 14 kHz for 10 s intervals. Instantaneous force was related to displacement via the Hookean trap stiffness k, assuming an isotropic response $\hat{\alpha}(x, y) = k$, so that $F_i = k\Delta r_i$. By integrating the calibrated force profiles (*SI Appendix*, Fig. S2), we obtained the corresponding "energy cup" that defines the effective cluster confinement.

Optical Particle Tracking. Particle tracking was performed at 65 Hz using a CCD camera (ORCA-spark, Hamamatsu), synchronized with force acquisition (14 kHz). Bacterial positions in the x-y trap plane, $\mathbf{r}_j(t) = (x_j, y_j)$, and their local optical densities w_j were extracted using Multiple Particle Tracking (MPT) with the SURF algorithm (53), with ∼100 nm spatial precision. Trajectories were recast into the cluster center-of-mass, $\mathbf{r}_{CM}(t) = \sum_j w_j \mathbf{r}_j(t) \big/ \sum_j w_j$, and displacements were computed as $\Delta\mathbf{r}(t_i) = \mathbf{r}(t_i + \Delta t) - \mathbf{r}(t_i)$ with $\Delta t = 0.015$ s, synchronized with the simultaneously acquired force signals. This establishes a one-degree-of-freedom mapping in which center-of-mass displacements $\Delta\mathbf{r}_i$ correspond to the net forces $\mathbf{F}_i$ measured by the trap in PMM mode.

Stochastic Force Correlations. We adapted the analysis of Battle et al. (11) to characterize fluctuating force trajectories in coarse-grained phase space (CGPS). Force components (F_x, F_y) were converted into probability fluxes $\mathbf{J}(F_x, F_y)$ under a normalized steady-state distribution $P(F_x, F_y)$. To identify dissipative features, we applied Helmholtz-Hodge decomposition, $\mathbf{F} = \mathbf{F}_{cons} + \mathbf{F}_{diss}$ (68), separating conservative forces associated with energy storage from dissipative forces that break detailed balance and generate entropy. Curl in CGPS, $\Omega = \nabla \times \mathbf{F}_{diss}$, quantified irreversibility, with flux strength approximated as $\mathbf{J} \propto \Omega\, \Upsilon\, \hat{\omega}$, where $\Upsilon = \langle d\mathbf{r}/d\theta \rangle$ and $\hat{\omega}$ is the angular velocity. Bootstrapping was used to assess statistical robustness.

Stochastic Energetics. Work was computed using discrete Itô calculus as $\Delta W_i = \mathbf{F}_i \circ \Delta\mathbf{r}_i$, where ∘ denotes Stratonovich multiplication. Dissipated power was quantified along the frictional pathway as $\tilde{Q}(t) = -\zeta \int_0^t \mathbf{v}^2 dt'$ under Newtonian friction $\mathbf{F}_{frict} = -\zeta\mathbf{v}$. Global energy conservation, $\Delta E = \tilde{W} + \tilde{Q} = 0$, allowed estimation of ensemble-averaged power dissipation $\mathcal{P} = \langle \Delta\tilde{W}/\Delta t \rangle = -\langle \Delta\tilde{Q}/\Delta t \rangle$ (16). The entropy production rate was computed as $\sigma = \langle dQ/dt \rangle / T$ under isothermal conditions (29), linking measured fluctuations to irreversible thermodynamic costs.

Statistical Analysis. Data are reported as mean ± SD from at least three biological replicates. Normally distributed datasets were compared using one-way ANOVA or Student's *t* test. Significance thresholds were $*P \leq 0.05$, $**P \leq 0.01$, $***P \leq 0.001$. All statistical analyses were performed using Prism 8.0 (GraphPad).

Data, Materials, and Software Availability. The raw force time series, representative raw videos, and the analysis software (MATLAB code/scripts) used to generate the results and figures are publicly available in a dedicated GitHub repository (69). An archived, citable snapshot of this repository is deposited in Zenodo (70) to ensure long-term preservation. All other data are included in the article and/or supporting information.

ACKNOWLEDGMENTS. We gratefully acknowledge Félix Ritort (University of Barcelona, Spain) for critical reading and insightful comments on the manuscript. We also thank A. Farré, O. Nos, and F. Catalá (IMPETUX SL) for their technical assistance with the SENSOCELL Optical Tweezer system. Special thanks go to Dr. Ignacio Vírseda-Chamorro (Hospital Central de la Defensa Gómez Ulla CSVE, Spain) for providing *P. mirabilis* samples. We further appreciate valuable discussions with Luis Dinis (Complutense University, Madrid, Spain) and David Lacoste (ESPCI, Paris, France). This work was supported by the Spanish Ministry of Science and Innovation–AEI (Grants PID2019-108391RB-I00, TED2021-132296B-C52 and CPP2024-011880) and by the Comunidad de Madrid (Grants Y2018/BIO-5207 and S2018/NMT-4389) (all to F.M.). Additional support to N.C. was provided by Grant CNS2023-143803 funded by MICIU/AEI/10.13039/501100011033 and by the European Union NextGeneration EU/PRTR (APC support).

Author affiliations: [a]Departamento de Química Física, Universidad Complutense de Madrid, Madrid 28040, Spain; [b]Cancer Division, Translational Biophysics, Instituto de Investigación Sanitaria Hospital Doce de Octubre (Imas12), Madrid 28041, Spain; [c]Escuela de Arquitectura y Tecnologia, Universidad San Jorge, Zaragoza 50830, Spain; [d]Facultad HM de Ciencias de la Salud, Universidad Camilo José Cela, Villanueva de la Cañada, Madrid 28692, Spain; [e]Instituto de Investigación Sanitaria HM Hospitales, Madrid 28015, Spain; [f]Instituto de Investigaciones Biosanitarias, Universidad Francisco de Vitoria, Pozuelo de Alarcón, Madrid 28223, Spain; and [g]Departamento de Estructura de la Materia, Física Térmica y Electrónica, Universidad Complutense de Madrid, Madrid 28040, Spain

1. L. Boltzmann, Weitere studien über das wärmegleichgewicht unter gasmolekülen. *Sitzungsber. Akad. Wiss.* **66**, 275–370 (1872).
2. S. Chandrasekhar, Stochastic problems in physics and astronomy. *Rev. Mod. Phys.* **15**, 1 (1943).
3. Q. A. Wang, Maximum entropy change and least action principle for nonequilibrium systems. *Astrophys. Space Sci.* **305**, 273–281 (2006).
4. K. Sekimoto, Langevin equation and thermodynamics. *Prog. Theor. Phys. Suppl.* **130**, 17–27 (1998).

5. C. Jarzynski, Nonequilibrium equality for free energy differences. *Phys. Rev. Lett.* **78**, 2690–2693 (1997).
6. G. E. Crooks, Entropy production fluctuation theorem and the nonequilibrium work relation for free energy differences. *Phys. Rev. E* **60**, 2721–2726 (1999).
7. U. Seifert, Stochastic thermodynamics, fluctuation theorems and molecular machines. *Rep. Progr. Phys.* **75**, 126001 (2012).
8. S. Ciliberto, Experiments in stochastic thermodynamics: Short history and perspectives. *Phys. Rev. X* **7**, 021051 (2017).
9. L. Peliti, S. Pigolotti, *Stochastic Thermodynamics: An Introduction* (Princeton University Press, 2021).
10. C. Bechinger *et al*., Active particles in complex and crowded environments. *Rev. Mod. Phys.* **88**, 045006 (2016).
11. C. Battle *et al*., Broken detailed balance at mesoscopic scales in active biological systems. *Science* **352**, 604–607 (2016).
12. D. A. Egolf, Equilibrium regained: From nonequilibrium chaos to statistical mechanics. *Science* **287**, 101–104 (2000).
13. I. Prigogine, *Non-Equilibrium Statistical Mechanics* (Interscience, 1962).
14. G. T. Landi, M. Paternostro, Irreversible entropy production: From classical to quantum. *Rev. Mod. Phys.* **93**, 035008 (2021).
15. I. Di Terlizzi *et al*., Variance sum rule for entropy production. *Science* **383**, 971–976 (2024).
16. K. Sekimoto, *Stochastic Energetics* (Springer, Berlin–Heidelberg, 2010).
17. C. Dieball, A. Godec, Thermodynamic bounds on generalized transport: From single-molecule to bulk observables. *Phys. Rev. Lett.* **133**, 067101 (2024).
18. J. Li, J. M. Horowitz, T. R. Gingrich, N. Fakhri, Quantifying dissipation using fluctuating currents. *Nat. Commun.* **10**, 1666 (2019).
19. I. Aoki, Entropy production in living systems: From organisms to ecosystems. *Thermochim. Acta* **250**, 359–370 (1995).
20. P. Martin, A. Hudspeth, F. Jülicher, Comparison of a hair bundle's spontaneous oscillations with its response to mechanical stimulation reveals the underlying active process. *Proc. Natl. Acad. Sci. U.S.A.* **98**, 14380–14385 (2001).
21. H. Turlier *et al*., Equilibrium physics breakdown reveals the active nature of red blood cell flickering. *Nat. Phys.* **12**, 513–519 (2016).
22. C. W. Lynn, E. J. Cornblath, L. Papadopoulos, M. A. Bertolero, D. S. Bassett, Broken detailed balance and entropy production in the human brain. *Proc. Natl. Acad. Sci. U.S.A.* **118**, e2109889118 (2021).
23. P. J. Foster, collaborators, Dissipation and energy propagation across scales in an active cytoskeletal material. *Proc. Natl. Acad. Sci. U.S.A.* **120**, e2214094120 (2023).
24. E. M. Purcell, Life at low Reynolds number. *Am. J. Phys.* **45**, 3–11 (1977).
25. U. Lucia, Bioengineering thermodynamics of biological cells. *Theor. Biol. Med. Model.* **12**, 1–16 (2015).
26. N. S. Goel, N. Richter-Dyn, *Stochastic Models in Biology* (Elsevier, 2016).
27. M. E. Cates, J. Tailleur, Motility-induced phase separation. *Annu. Rev. Condens. Matter Phys.* **6**, 219–244 (2015).
28. A. E. Patteson, A. Gopinath, P. E. Arratia, The propagation of active-passive interfaces in bacterial swarms. *Nat. Commun.* **9**, 5373 (2018).
29. D. J. Skinner, J. Dunkel, Improved bounds on entropy production in living systems. *Proc. Natl. Acad. Sci. U.S.A.* **118**, e2024300118 (2021).
30. Y. Deng, D. R. Beahm, S. Ionov, R. Sarpeshkar, Measuring and modeling energy and power consumption in living microbial cells with a synthetic ATP reporter. *BMC Biol.* **19**, 101 (2021).
31. P. E. Schavemaker, M. Lynch, Flagellar energy costs across the tree of life. *eLife* **11**, e77266 (2022).
32. J. P. Armitage, R. M. Berry, Assembly and dynamics of the bacterial flagellum. *Annu. Rev. Microbiol.* **74**, 181–200 (2020).
33. M. D. Manson, P. Tedesco, H. C. Berg, F. M. Harold, C. Van der Drift, A protonmotive force drives bacterial flagella. *Proc. Natl. Acad. Sci. U.S.A.* **74**, 3060–3064 (1977).
34. S. E. Tusk, N. J. Delalez, R. M. Berry, Subunit exchange in protein complexes. *J. Mol. Biol.* **430**, 4557–4579 (2018).
35. G. Gottschalk, *Regulation of Bacterial Metabolism* (Springer, 1986).
36. E. Lauga, Bacterial hydrodynamics. *Annu. Rev. Fluid Mech.* **48**, 105–130 (2016).
37. J. A. Nirody, Y. R. Sun, C. J. Lo, The biophysicist's guide to the bacterial flagellar motor. *Adv. Phys. X* **2**, 324–343 (2017).
38. A. Kitao, H. Hata, Molecular dynamics simulation of bacterial flagella. *Biophys. Rev.* **10**, 617–629 (2018).
39. D. L. Koch, G. Subramanian, Collective hydrodynamics of swimming microorganisms: Living fluids. *Annu. Rev. Fluid Mech.* **43**, 637–659 (2011).
40. J. Elgeti, R. G. Winkler, G. Gompper, Physics of microswimmers-single particle motion and collective behavior: A review. *Rep. Progr. Phys.* **78**, 056601 (2015).
41. C. Jones *et al*., Stochastic force dynamics of the model microswimmer *Chlamydomonas reinhardtii*: Active forces and energetics. *Phys. Rev. E* **103**, 032403 (2021).
42. C. J. Bustamante, Y. R. Chemla, S. Liu, M. D. Wang, Optical tweezers in single-molecule biophysics. *Nat. Rev. Methods Prim.* **1**, 25 (2021).
43. A. Farré, M. Montes-Usategui, A force detection technique for single-beam optical traps based on direct measurement of light momentum changes. *Opt. Express* **18**, 11955–11968 (2010).
44. A. Farré, F. Marsà, M. Montes-Usategui, *Beyond the hookean spring model: Direct measurement of optical forces through light momentum changes*, A Gennerich, Ed. (Springer, New York, New York, NY, 2017), pp. 41–76.
45. M. Polin, I. Tuval, K. Drescher, J. P. Gollub, R. E. Goldstein, Chlamydomonas swims with two "gears" in a eukaryotic version of run-and-tumble locomotion. *Science* **325**, 487–490 (2009).
46. J. Tailleur, M. E. Cates, Statistical mechanics of interacting run-and-tumble bacteria. *Phys. Rev. Lett.* **100**, 218103 (2008).
47. M. Mell, F. Monroy, A gradient-based, GPU-accelerated, high-precision contour-segmentation algorithm with application to cell membrane fluctuation spectroscopy. *PLoS One* **13**, e0207376 (2018).
48. S. Salinas-Almaguer *et al*., Membrane rigidity regulates *E. coli* proliferation rates. *Sci. Rep.* **12**, 933 (2022).
49. S. Shinkai, Y. Togashi, Energetics of single active diffusion trajectories. *EPL* **105**, 30002 (2014).
50. Z. Zhang, T. E. Kimkes, M. Heinemann, Manipulating rod-shaped bacteria with optical tweezers. *Sci. Rep.* **9**, 19086 (2019).
51. G. Soni, B. J. Ali, Y. Hatwalne, G. Shivashankar, Single particle tracking of correlated bacterial dynamics. *Biophys. J.* **84**, 2634–2637 (2003).
52. R. Rodríguez-García *et al*., Direct cytoskeleton forces cause membrane softening in red blood cells. *Biophys. J.* **108**, 2794–2806 (2015).
53. D. Herráez-Aguilar *et al*., Multiple particle tracking analysis in isolated nuclei reveals the mechanical phenotype of leukemia cells. *Sci. Rep.* **10**, 6707 (2020).
54. T. Speck, Stochastic thermodynamics for active matter. *Europhys. Lett.* **114**, 30006 (2016).
55. D. Mandal, K. Klymko, M. R. DeWeese, Entropy production and fluctuation theorems for active matter. *Phys. Rev. Lett.* **119**, 258001 (2017).
56. C. E. Armbruster, H. L. Mobley, M. M. Pearson, Pathogenesis of proteus mirabilis infection. *EcoSal Plus* **8**, 10–1128 (2018).
57. C. Douglas, Measurement of proteus cell motility during swarming. *J. Med. Microbiol.* **12**, 195–200 (1979).
58. T. Matsuyama *et al*., Dynamic aspects of the structured cell population in a swarming colony of proteus mirabilis. *J. Bacteriol.* **182**, 385–393 (2000).
59. C. Y. Chen *et al*., Proteus mirabilis urinary tract infection and bacteremia: Risk factors, clinical presentation, and outcomes. *J. Microbiol. Immunol. Infect.* **45**, 228–236 (2012).
60. C. E. Armbruster, H. L. Mobley, Merging mythology and morphology: The multifaceted lifestyle of proteus mirabilis. *Nat. Rev. Microbiol.* **10**, 743–754 (2012).
61. H. H. Tuson, M. F. Copeland, S. Carey, R. Sacotte, D. B. Weibel, Flagellum density regulates proteus mirabilis swarmer cell motility in viscous environments. *J. Bacteriol.* **195**, 368–377 (2013).
62. C. W. Gardiner *et al*., *Handbook of Stochastic Methods* (Springer Berlin, 1985), vol. 3.
63. A. Ashkin, J. M. Dziedzic, Optical trapping and manipulation of viruses and bacteria. *Science* **235**, 1517–1520 (1987).
64. M. E. Cates, "Active field theories" in *Active Matter and Nonequilibrium Statistical Physics, Les Houches Summer School*, G. Gompper, M. C. Marchetti, J. Tailleur, Eds. (Oxford University Press, Oxford, UK, 2022), vol. **112**.
65. G. E. Piñas, V. Frank, A. Vaknin, J. S. Parkinson, The source of high signal cooperativity in bacterial chemosensory arrays. *Proc. Natl. Acad. Sci. U.S.A.* **113**, 3335–3340 (2016).
66. L. D. Landau, E. M. Lifshitz, *Fluid Mechanics: Volume 6* (Elsevier, 1987), vol. 6.
67. K. C. Leptos, M. Chioccioli, S. Furlan, A. I. Pesci, R. E. Goldstein, Phototaxis of *Chlamydomonas arises* from a tuned adaptive photoresponse shared with multicellular volvocine green algae. *Phys. Rev. E* **107**, 014404 (2023).
68. R. Dautray, J. L. Lions, *Spectral Theory and Applications, Mathematical Analysis and Numerical Methods for Science and Technology* (Springer-Verlag, 1990), vol. 3.
69. C. Luque-Rioja *et al*., Stochastic-motility-energetics-reveals-cooperative-bacterial-swarming-in-optical-tweezers. GitHub. https://github.com/claraluq/Stochastic-motility-energetics-reveals-cooperative-bacterial-swarming-in-optical-tweezers. Deposited 30 December 2025.
70. C. Luque-Rioja *et al*., claraluq/Stochastic-motility-energetics-reveals-cooperative-bacterial-swarming-in-optical-tweezers: Data and code for stochastic motility in optically trapped bacterial swarms. Zenodo. https://doi.org/10.5281/zenodo.18095022. Deposited 30 December 2025.